

Mn Nanoparticles Encapsulated within Mesoporous Helical N-Doped Carbon Nanotubes as Highly Active Air Cathode for Zinc–Air Batteries

Qing Dong, Hui Wang, Shan Ji,* Xuyun Wang, Quanbing Liu, Daniel J. L. Brett, Vladimir Linkov, and Rongfang Wang*

The practical application of clean energy conversion and storage technologies, such as fuel cells and metal–air batteries, have been significantly impeded by the high cost and scarcity of precious metal catalysts used for the oxygen reduction reaction (ORR). Transitional metal/carbon compounds are a promising alternative to precious metal catalysts for the ORR. Herein, Mn nanoparticles encapsulated within mesoporous helical N-doped carbon nanotubes (Mn@HNCNTs) are developed as highly active ORR catalysts. In terms of the onset potential and half-wave potential for ORR, the optimized Mn@HNCNTs exhibit an excellent ORR performance, which is comparable to Pt/C. When the Mn@HNCNTs are assembled as air cathodes, with zinc foil as the anode in primary zinc–air cells, the obtained cell delivers a higher cell voltage and capacity than the zinc–air cell using Pt/C as the air cathode, as well as many reported cells using TM/CNT-based air cathodes. The electrocatalytic performance in the zinc–air cell demonstrates that Mn@HNCNTs have great potential for use as ORR catalysts in metal–air batteries.

1. Introduction

Due to the rapid depletion of fossil fuels and the environmental problems caused by using them, tremendous research efforts have contributed to developing renewable energy sources and advanced technologies for clean energy conversion and storage, such as fuel cells, metal–air batteries, and water electrolyzers.^[1–4] Electrochemical reactions essential to the effective operation of many clean energy conversion and storage technologies include the hydrogen oxidation reaction (HOR), which occurs at the anode of fuel cells^[5] and the oxygen reduction reaction (ORR) at the cathode of fuel cells and metal–air batteries.^[6,7] Unfortunately, the ORR is a complex multi-electron process, and its sluggish kinetics significantly limits the performance of these clean energy technologies, requiring platinum group metals (PGMs) to catalyze

the ORR to achieve high efficiency.^[8–10] However, the scarcity, high cost, and low selectivity of PGM catalysts seriously impede their large-scale application. Therefore, to develop non-PGM catalysts with high ORR activity and durability is of great interest.

Recently, heteroatom-doped carbons have attracted much research attention as a promising alternative to PGM catalysts for ORR due to their high activity, durability, and low-cost.^[11–13] In order to replace the PGM catalysts and use as ORR catalysts for practical applications, the main challenge is that the ORR performance of these heteroatom-doped carbons needs to be further improved to be competitive.^[14,15] For the nitrogen-doped (N-doped) carbon catalysts, it was found that their electrocatalytic properties can be effectively enhanced by integrating transitional metal nanoparticles (TMNs) into the matrix of N-doped carbon materials. In such a structure, the aggregation of TMNs can be efficiently restrained and exhibit long durability. In addition to efficiently avoiding particle aggregation, this combination also improves electrocatalytic activity due to the synergistic effect between carbon and transition metal particles.^[16] For instance, CoSe nanoparticles incorporated into mesoporous N-doped carbon was developed as an ORR catalyst and it was found that the CoSe modified N-doped carbon exhibited a much better ORR performance than its N-doped carbon counterpart.^[17]


Q. Dong, Prof. H. Wang, Prof. X. Wang, Prof. R. Wang
College of Chemical Engineering
Qingdao University of Science and Technology
Qingdao 266042, China
E-mail: rfwang@qust.edu.cn

Prof. S. Ji
College of Biological
Chemical Science and Chemical Engineering
Jiaxing University
Jiaxing 314001, China
E-mail: jishan@mail.zjxu.edu.cn

Prof. Q. Liu
School of Chemical Engineering and Light Industry
Guangdong University of Technology
Guangzhou 510006, China

Prof. D. J. L. Brett
Electrochemical Innovation Lab
Department of Chemical Engineering
University College London
London WC1E 7JE, UK

Prof. V. Linkov
South African Institute for Advanced Materials Chemistry
University of the Western Cape
Cape Town 7535, South Africa

 The ORCID identification number(s) for the author(s) of this article can be found under <https://doi.org/10.1002/adsu.201900085>.

DOI: 10.1002/adsu.201900085

N-doped mesoporous carbon containing dispersed Fe-N_x species has been prepared and tested as an ORR and oxygen evolution reaction bifunctional catalyst; the obtained catalyst demonstrates electrocatalytic performance comparable to Pt/C and RuO₂ catalysts in zinc–air batteries.^[18] Recently, it was also found that the ability to tune and engineer the morphology and microstructure of the N-doped carbons have is an effective approach to improving the electrocatalytic performance.^[19,20]

It has been proven that certain nanomaterials, for instance, nanotubes, nanosheets, nanoribbons, hierarchical nanostructure, etc., can act as building blocks to design and construct catalysts with unique physical and electrocatalytic properties.^[21] Helicity is a common structure in nature, and the nanomaterials with helical morphology could be another building block to achieve high-performance electrocatalysts in the development of ORR catalysts. In 1994, helical carbon nanotubes were developed by Amelinckx et al. and showed remarkable chemical features with great potential applications.^[22] Compared to 1D straight carbon nanotubes, the reports on helical carbon nanotubes as ORR catalysts are very rare. It will be interesting to develop TMNs/N-doped carbon materials with a helical structure as ORR catalysts from a scientific development point of view.

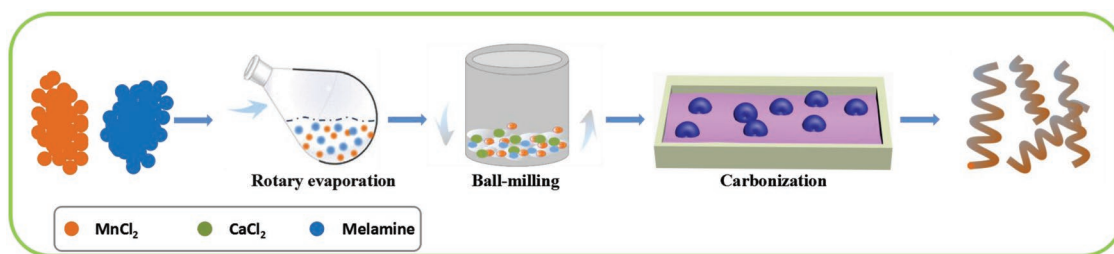
In this study, Mn nanoparticles encapsulated helical N-doped carbon nanotubes (Mn@HNCNTs) were designed and synthesized as the ORR electrocatalyst via a molten-salt method at high temperature, as presented in Figure S1 in the Supporting Information. During the synthetic procedure, melamine was adopted as the nitrogen and carbon sources to form an N-doped carbon matrix, and MnCl₂ was used to form Mn nanoparticles in the molten-salt media of calcium chloride. The obtained Mn@HNCNTs were employed as the building blocks to fabricate the air cathode for the zinc–air battery. The Mn@HNCNTs were integrated into a fully functional zinc–air cell to evaluate its performance in under real-world conditions, which exhibited a high open-circuit voltage and cell voltage at 10 mA cm⁻², superior to the state-of-the-art Pt/C (20 wt%). Owing to its unique structure, the Mn@HNCNTs exhibited excellent electrocatalytic performance for ORR, which paves the way for developing N-doped carbon materials with helical morphology for practical applications in clean energy conversion and storage.

2. Results and Discussion

The formation of Mn@HNCNTs is schematically illustrated in Scheme 1. Initially, the manganese chloride was reduced to form Mn nanoparticles during the decomposition of melamine in the molten-salt medium at high temperature. These

newly formed Mn nanoparticles with a certain particle size then acted as the catalyst, and CNTs were grown on Mn nanoparticles. Due to the anisotropy of the lattice planes available on the surface of these Mn nanoparticles, with diameter less than 100 nm, the growth rate of CNTs was different at the interface of carbon sources and Mn catalysts, which caused the nanotube formed on the catalyst to bend and form CNTs with helical morphology. Since the Mn nanoparticles acted as the catalysts for the formation of CNTs, the Mn nanoparticles were well wrapped by carbon materials and located in one end of the obtained CNTs, which could be proven by the following physical characterization.

Initially, the morphology of the obtained Mn@HNCNTs-2 was investigated by scanning electron microscopy (SEM) analysis. As shown in Figure 1a, many carbon nanotubes with various diameters and morphologies were observed. The diameters of these carbon tubes are in the range of 300 nm to 2 μm. The carbon tubes with the morphologies of helical, straight, and coil tubes are presented in Figure 1a, implying there are various crystal planes formed on these Mn nanoparticle catalysts. In the zoom-in SEM images shown in Figure 1b,c, it can be seen that the surface of most of the carbon tubes are not smooth and exhibit wrinkles and defects. The detailed microstructure of the obtained helical CNTs was further analyzed by transmission electron microscopy (TEM). The diameter of the helical carbon nanotubes (HCNTs) was quite uniform (Figure 1d) and the structure information was also shown in this figure. Compared with the HCNTs shown in Figure 1e, the spiral diameter and distance of the HCNTs were different from the HCNTs presented in Figure 1d, namely various sized HCNTs were formed. As shown in Figure 1e, both ends of the HCNT were opened up, which could allow access of reactant to the internal surface of the HCNT. Occasionally, “stacked-cup” HCNTs were also observed, which further demonstrated the variety of CNTs synthesized by this method. In the inset of Figure 1e, it was observed that a rough surface with many wrinkles was formed on HCNT, which could provide more active sites for the catalytic reactions. In the high-resolution TEM image of Mn@HNCNTs-2, the Mn nanoparticle was completely wrapped by carbon materials, which could be proven by the *d*-spacing distance of lattice fringe shown in the inset of Figure 1f. Figure 1f indicates that the Mn nanoparticles acted as the catalyst for forming the HCNTs. In the SEM image of the Mn@HNCNTs sample prepared without the molten-salt medium of CaCl₂, a small amount of HCNT was observed in the SEM (Figure S2, Supporting Information), and the degree of helix formation is relatively low, indicating that CaCl₂ plays a critical role in the formation of HCNTs. The element



Scheme 1. Schematic illustration of the formation of Mn@HNCNTs.

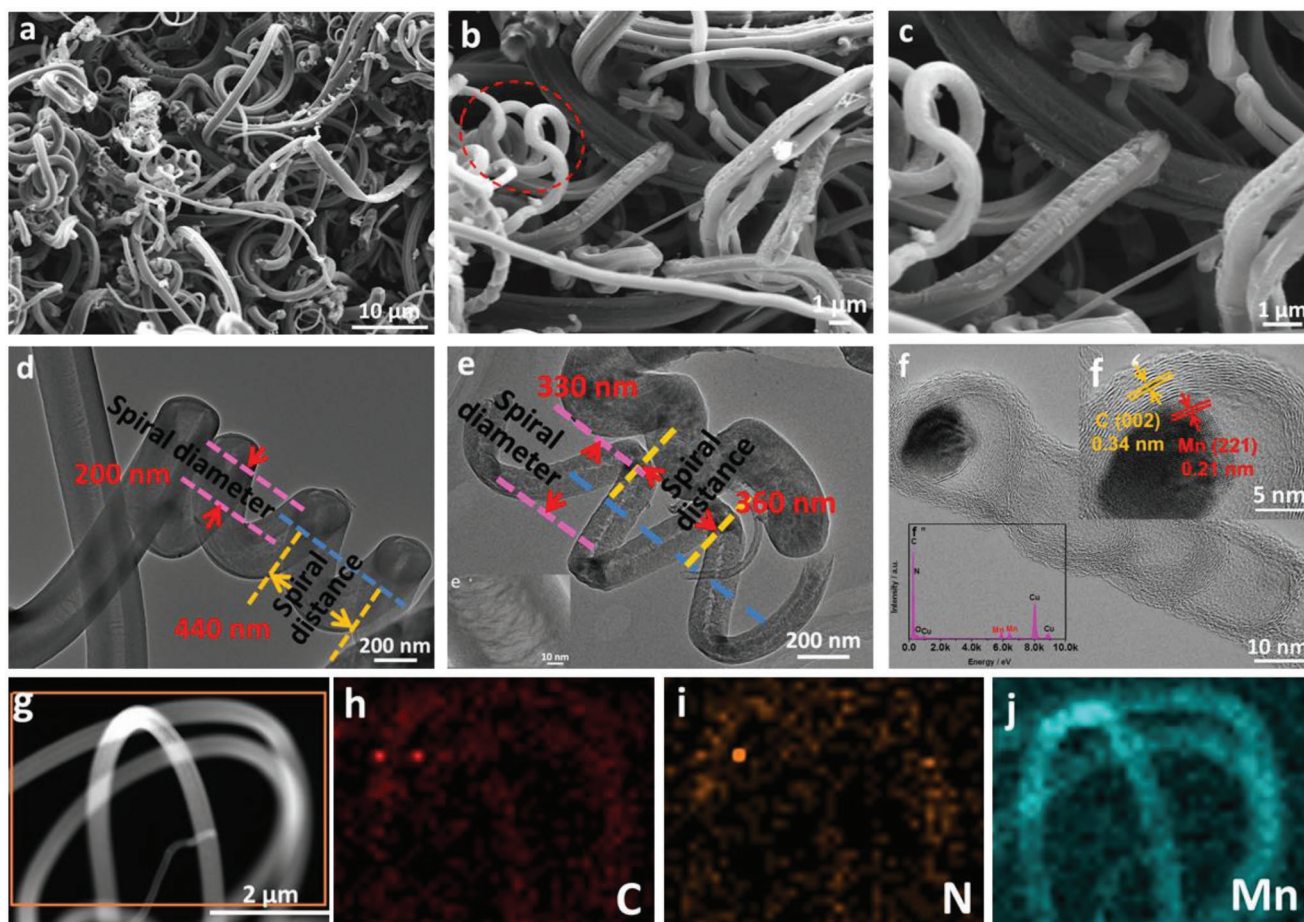


Figure 1. a–c) SEM images of Mn@HNCNTs-2; d–f) TEM images of Mn@HNCNTs-2; f') EDX, g) STEM, elemental mapping images of h) C, i) N, and j) Mn.

composition was analyzed and found that the percentage of C, N, and Mn in Mn@HNCNTs-2 are 81.4, 5.5, and 14.1 wt%, respectively.

During the experiments, it was found that the average particle size of the MnCl₂ catalysts related to the ball-milling times had a significant impact on the obtained morphology. Therefore, the effect of ball-milling times for the MnCl₂ catalysts on the morphology was investigated. **Figure 2** shows the particle size distribution of the MnCl₂ samples just after ball-milling. In the sample of MnCl₂ without ball-milling, its particle size distribution was centered at ≈255 nm (Figure 2a). Most of the particles formed in Mn@HNCNTs-0 were irregular, but a few CNTs were also found in the SEM image (Figure 2b), indicating that Mn nanoparticles could catalyze the formation of CNTs. After the MnCl₂ sample was ball-milled for 6 h, there is a clear drop in the particle size, and, for most of the MnCl₂ particles, their sizes were located at 164 nm (Figure 2c); some coiled CNTs were formed but most of the carbon products were still irregular (Figure 2d). Figure 2e is the particle size distribution of MnCl₂, which had been ball-milled for 12 h. Compared to the sample with 6 h ball-milling, the particle sizes were further decreased and more than 80% of particles were located in the range of ≈50–60 nm. Many CNTs with the helical, coil, and straight forms were observed in the obtained sample, and only

a few irregular particles are seen in Figure 2f. These results suggest that MnCl₂ particles with a small particle size can facilitate the formation of HCNTs. When the ball-milling time was further increased to 18 h, it was found that the particle size actually increased due to the aggregation. Accordingly, the HCNTs formed Mn@HNCNTs-3 are quite short and accompanied by many irregular particles. The above results indicate that the small particle size of MnCl₂, with a narrow particle size distribution (50–60 nm), favors the formation of HCNT. A similar phenomenon was also observed by Qian and co-workers when the ball-milling time was too long.^[23]

Raman spectroscopy was applied to analyze the carbon structure formed on these Mn@HNCNTs samples (**Figure 3a**). There are two peaks shown in all Raman spectra of all four samples (Figure 3a), namely a D-band at ≈1343 cm⁻¹ originating from heteroatoms, vacancies, heptagon-pentagon pairs, kinks, and the disordered structure of carbon and a G-band at ≈1589 cm⁻¹ arising from the sp²-hybridized graphite.^[24] Usually, the ratio of the intensity of these two bands (I_D/I_G) is used to represent the density of surface defects, meaning that higher defect structure available on the surface of carbon results in a higher value of the I_D/I_G ratio. The I_D/I_G ratios of these Mn@HNCNTs samples were presented as the inset of Figure 3a. It shows that the Mn@HNCNTs-2 has the highest I_D/I_G value, indicating that

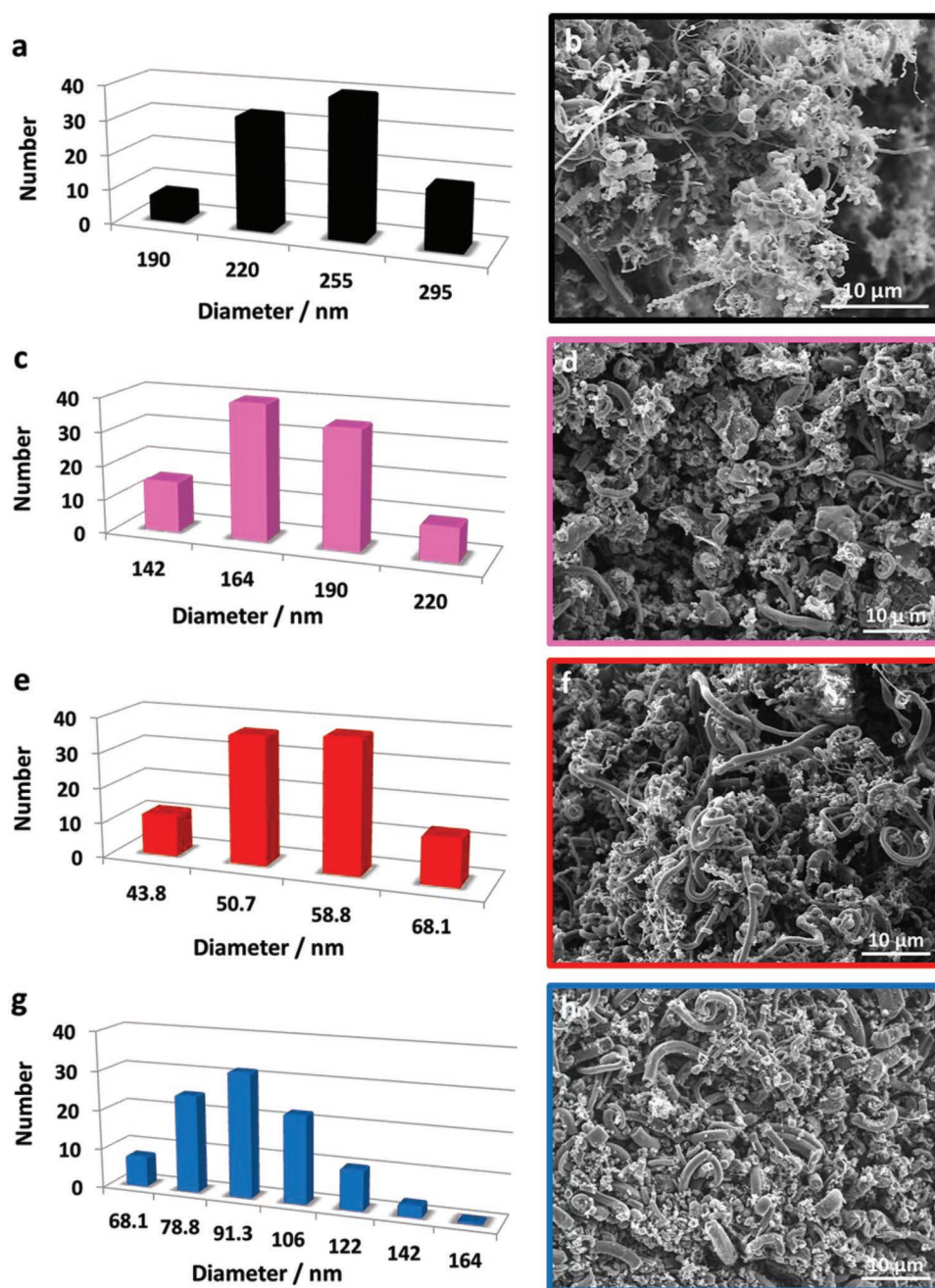


Figure 2. The particle size distribution of the MnCl_2 catalyst with various ball-milling times, i.e., a) 0 h, c) 6 h, e) 12 h, and g) 18 h. Corresponding SEM image of b) Mn@HNCNTs-0, d) Mn@HNCNTs-1, f) Mn@HNCNTs-2, and h) Mn@HNCNTs-3.

the density of surface defects on Mn@HNCNTs-2 is the highest one among all the prepared Mn@HNCNTs samples. As shown in the inset of Figure 1e, the surface of Mn@HNCNTs-2 was quite rough and wrinkled. The number of HNCNTs formed in the Mn@HNCNTs-2 was also the highest among all the four samples (Figure 2), which could be the reason there are more surface defects available on Mn@HNCNTs-2. Higher surface defects usually represent higher active sites exposed on the surface. Therefore, it was expected that the Mn@HNCNTs-2 will exhibit better electrocatalytic performance than other Mn@HNCNTs samples. X-ray diffraction (XRD) was further

employed to investigate the crystallinity of the obtained Mn@HNCNTs samples (Figure 3b). The peak at $\approx 26.2^\circ$ can be ascribed to the (002) plane of graphitic carbon,^[24] revealing the graphite was formed during the pyrolysis process. The intensity of C (002) peak of Mn@HNCNTs-2 is obviously higher than that of other Mn@HNCNTs samples due to the relative high graphitization of Mn@HNCNTs, consistent with the Raman results. The broad diffraction peak at $\approx 43.5^\circ$ observed on all XRD patterns of Mn@HNCNTs samples is the overlapping of the (101) plane of the carbon and the (221) plane of Mn. Compared to the standard XRD of Mn, the (320) and (321)

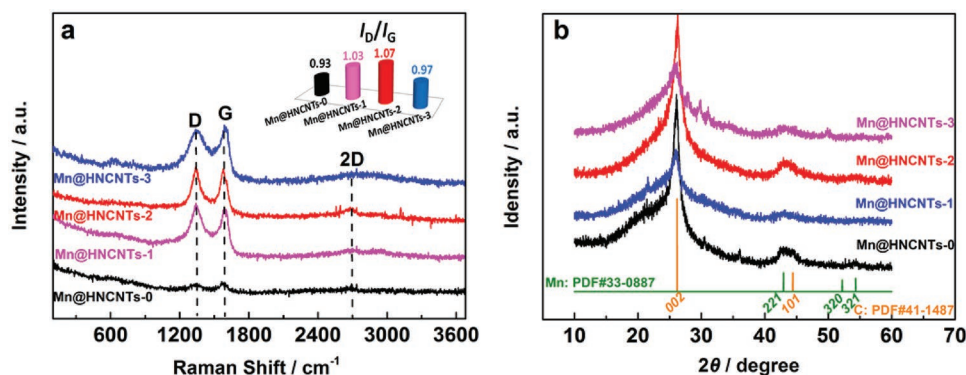


Figure 3. a) Raman spectra and b) XRD patterns of Mn@HNCNTs-0, Mn@HNCNTs-1, Mn@HNCNTs-2, and Mn@HNCNTs-3.

characteristic diffraction peaks of Mn were also observed in the XRD pattern of Mn@HNCNTs samples, indicating the formation of the Mn particles, which is agree well with the TEM observation presented in Figure 1f.

N_2 adsorption–desorption isotherms were carried out to study the porosity of Mn@HNCNTs-0, Mn@HNCNTs-1, Mn@HNCNTs-2, and Mn@HNCNTs-3. According to International Union of Pure and Applied Chemistry classification, the N_2 adsorption–desorption isotherms shown in Figure 4a indicate that the isotherms of these samples are type IV with a clear nitrogen uptake at the low relative pressure region and a hysteresis loop at the high relative pressure, suggesting that both micropores and mesopores existed in these samples.^[17] Figure 4b shows that the pore size distributions of these samples were mainly located at two regions, namely 3–10 and 15–20 nm. The specific surface areas of Mn@HNCNTs-0,

Mn@HNCNTs-1, Mn@HNCNTs-2, and Mn@HNCNTs-3 calculated by Brunauer–Emmett–Teller (BET) method were 150.1, 134.6, 424.6, and 223.2 $m^2 g^{-1}$, respectively. Due to the rough and wrinkled nature of the surface, as expected, Mn@HNCNTs-2 has the highest specific surface area among all four samples. Since some small pores are not accessible for the reactants, the external surface area, namely the real surface area available for reactions, is a critical parameter to evaluate the porosity, which can be calculated via the $V-t$ plots in the linear regions, typically between 0.2 and 0.5 P/P_0 .^[12] As shown in Figure 4c, Mn@HNCNTs-2 exhibited the largest external surface area among all the Mn@HNCNTs samples, as well as the largest pore volume (Figure 4d). BET results imply that, compared with other Mn@HNCNTs samples, Mn@HNCNTs-2 has the more exposed surface area and pore volume for the reactants. The specific surface area of Mn @HNCNTs-2 was also compared

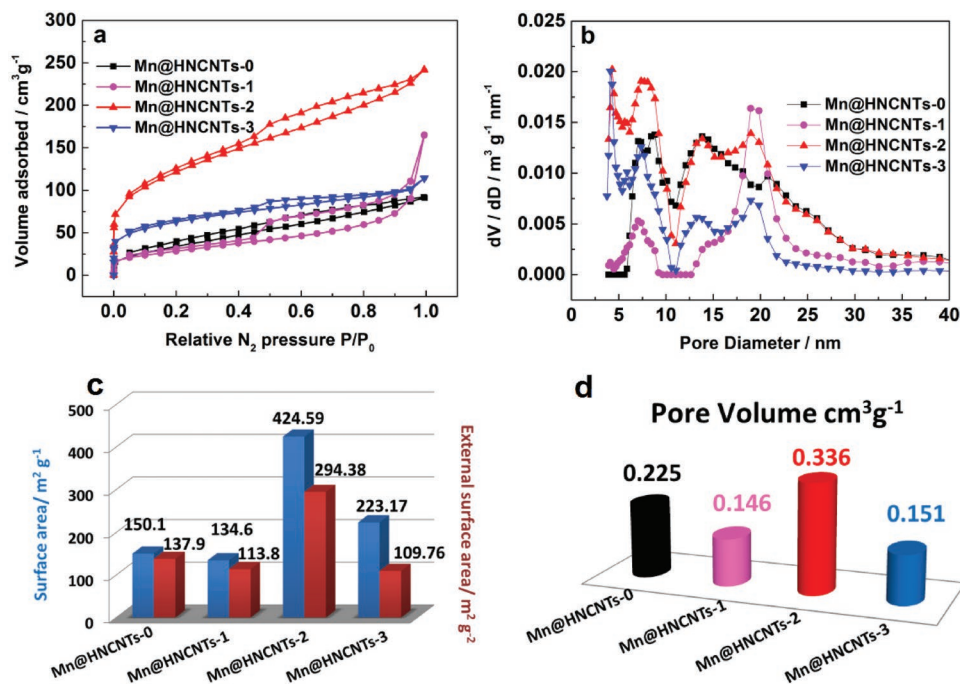


Figure 4. a) N_2 adsorption–desorption isotherms, b) corresponding pore size distributions, c) BET surface areas and d) pore volumes of Mn@HNCNTs-0, Mn@HNCNTs-1, Mn@HNCNTs-2, and Mn@HNCNTs-3.

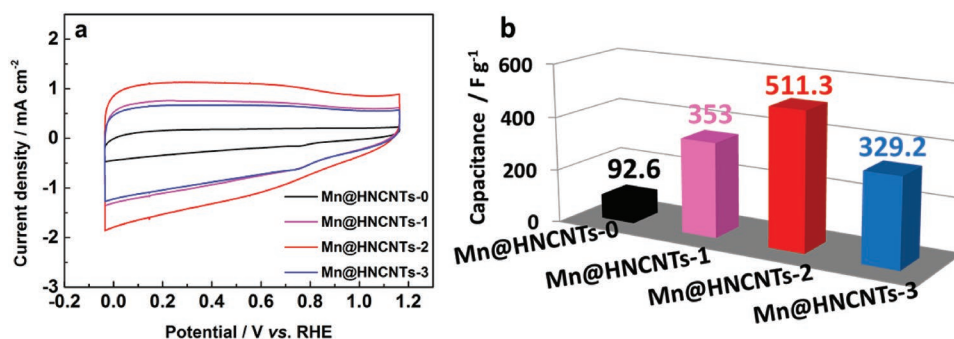


Figure 5. a) CV curves and b) capacitance of Mn@HNCNTs-0, Mn@HNCNTs-1, Mn@HNCNTs-2, and Mn@HNCNTs-3 in N₂-saturated 0.1 M KOH solution measured with a scan rate of 50 mV s⁻¹.

with some of the CNT-based ORR catalysts in Table S1 in the Supporting Information. The results show that the helical structure of Mn@HNCNTs-2 and the rough wrinkled surface can significantly increase the specific surface area of the catalyst.

The electrochemical surface areas of these Mn@HNCNTs can be evaluated by the electrochemical double-layer capacitance (EDLC), which can be calculated from the cyclic voltammetry (CV) analysis. In this case, the potential window of 0.036–1.164 V versus reversible hydrogen electrode (RHE) was chosen to avoid the Faradaic redox occurred during the CV measurement. Based on the CV curves, the EDLC of these Mn@HNCNTs samples can be calculated via the method reported by Wang and co-workers^[25] and shown in Figure 5. As expected, the Mn@HNCNTs-2 has a high capacitance of 511.3 F g⁻¹, much higher than the other three samples, indicating that there are more electrochemical active sites available on Mn@HNCNTs-2. The electrochemical surface areas of these Mn@HNCNTs were also evaluated based on the CVs

at different scanning rates (Figure S3a–d, Supporting Information). At 0.566 V (RHE), J_a – J_c versus voltage scan rates were plotted and are shown in Figure S3e in the Supporting Information, where the slope represents the electrochemical double-layer capacitance; corresponding capacitances rose concurrently with an increase in active surface sites concentrations: Mn@HNCNTs-0 (7.5 mF cm⁻²) < Mn@HNCNTs-3 (27.1 mF cm⁻²) < Mn@HNCNTs-1 (29.3 mF cm⁻²) < Mn@HNCNTs-2 (46.7 mF cm⁻²).

To evaluate the intrinsic electrocatalytic properties of the ORR, all prepared Mn@HNCNTs samples were investigated by linear sweep voltammetry (LSV) in O₂-saturated KOH solution, and all the obtained LSV curves were subtracted from the corresponding baselines obtained in N₂-saturated solution and benchmarked against the LSV curve of Pt/C, the state-of-the-art ORR catalyst. As illustrated in Figure 6a, the Mn@HNCNTs-2 exhibited the best ORR activity among all four Mn@HNCNTs samples, and its ORR LSV curve almost overlapped with the

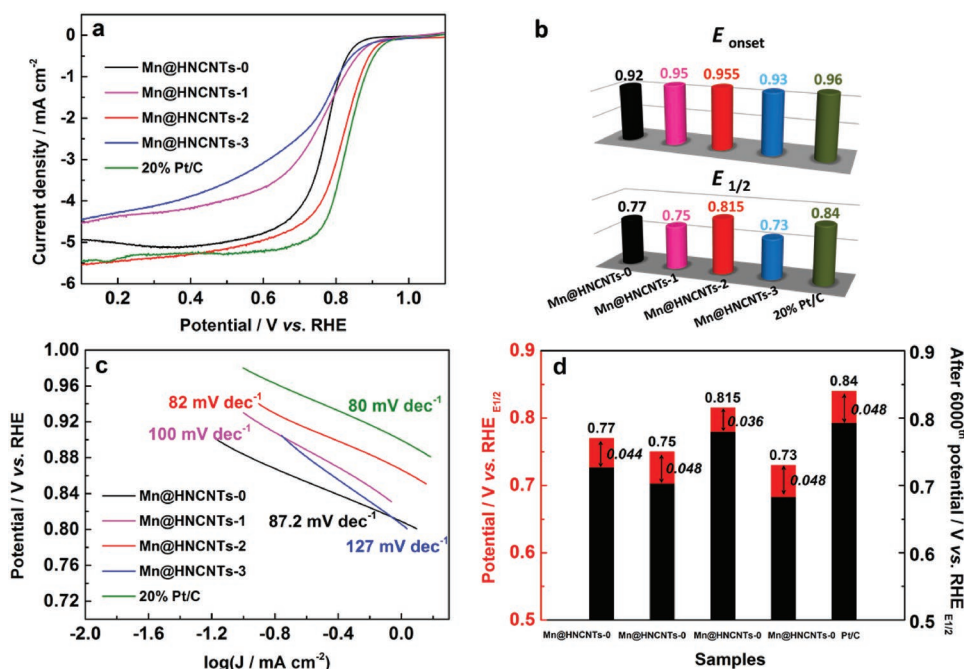


Figure 6. a) LSV curves for ORR on Mn@HNCNTs samples and Pt/C. b) Onset potential and half-wave potential for ORR. c) Their corresponding ORR Tafel plots. d) Drop in the half-wave potential of the ORR LSV curves after 6000th cycles.

LSV curve of Pt/C. The corresponding onset potential (E_{onset}) and half-wave potential ($E_{1/2}$) are displayed in Figure 6b, showing that the E_{onset} and $E_{1/2}$ of Mn@HNCNTs-2 were only 5 and 25 mV more negative than those of Pt/C, demonstrating the ORR activity of Mn@HNCNTs-2 was comparable to that of Pt/C. The highly electrochemical surface area could be the main reason the Mn@HNCNTs-2 exhibited high ORR activity. The E_{onset} and $E_{1/2}$ of Mn@HNCNTs-2 were also compared with those of many representative TM-based/CNT ORR catalysts reported in the literature (Table S2, Supporting Information). Mn@HNCNTs-2 has more positive E_{onset} and $E_{1/2}$ values than most of reported TM-based/CNT ORR catalysts, further indicating the high ORR activity of Mn@HNCNTs-2. The electrocatalytic kinetics of the ORR occurred on Mn@HNCNTs samples and Pt/C was further analyzed using the Tafel plots shown in Figure 6c. Usually, the lower Tafel slope represents the faster catalytic kinetics.^[26] The Tafel slope of Mn@HNCNTs-2 is 82 mV dec⁻¹, lower than the other three Mn@HNCNTs samples, due to its faster ORR catalytic kinetics, which could be attributed to its high electrochemical surface area and pore volume. The Tafel slope of Mn@HNCNTs-2 is even slightly lower than that of Pt/C, further proof of the fast catalytic kinetics. The ORR durability was also tested for these Mn@HNCNTs samples by LSV in oxygen-saturated KOH solution for 6000 continuous cycles (Figure 6d). The durability was evaluated by comparing the half-wave potential before and after the 6000 cycles (Figure 6d and Figure S4, Supporting Information). After 6000 continuous cycles, the half-wave potential of Mn@HNCNTs-2 shifted negatively by 36 mV, which was even lower than Pt/C (48 mV) in the KOH solution, namely possesses very good ORR stability. SEM and TEM analysis were also carried out to investigate the morphological change of Mn@HNCNTs-2 after the ORR stability test (Figure S5, Supporting Information). Compared to the SEM and TEM images of the fresh Mn@HNCNTs-2 (Figure 1), no obvious changes were observed after 6000 cycles of CV test, which further confirms that Mn@HNCNTs-2 is stable in ORR.

The electron transfer number of the ORR was also studied in an O₂ saturated KOH electrolyte at various rotation rates on a rotating electrode disc (RDE). As illustrated in Figure S6 in the Supporting Information, the ORR occurred on these Mn@HNCNTs samples, similar to Pt/C, followed the highly efficient four-electron pathway. The ORR mechanism of Mn@HNCNTs was also investigated by rotating ring disk electrode (RRDE) measurements (Figure S7, Supporting Information). In RRDE testing, the ring potential was set to 0.4 V. The percentage of HO₂⁻ and the electron transfer number are determined by the following equations

$$\text{HO}_2^- = 200 \times \frac{i_{\text{r}}/N}{i_{\text{d}} + i_{\text{r}}/N} \times 100\% \quad (1)$$

$$n = 4 \times \frac{i_{\text{d}}}{i_{\text{d}} + i_{\text{r}}/N} \quad (2)$$

where i_{d} is the disk current, i_{r} is the ring current, and N is the current collection efficiency of the Pt ring. N was determined to be 0.38 from the reduction of K₃Fe[CN]₆, which is consistent with the manufacture's value (0.37). As shown Figure S7 in the Supporting Information, the HO₂⁻ percentage produced by

the Mn@HNCNTs is 4.5% (obtained from Equation (1)), even lower than that of Pt/C (7%). The RRDE tests agree well with the results calculated from the Koutecky–Levich equation that the ORR electron transfer number of Mn@HNCNTs is close to 4 (based on Equation (2)).

The ORR performance of the Mn@HNCNTs-2 was evaluated under real-world conditions in a primary zinc–air cell, in which Mn@HNCNTs-2 was applied as the air cathode and zinc foil as the anode, with 6 M KOH as the electrolyte (Mn@HNCNTs cell). For comparison, a zinc–air cell using Pt/C as the cathode was also assembled (Pt/C cell). The Mn@HNCNTs-2 cell could deliver a stable open-circuit voltage at 1.57 V, higher than the Pt/C cell (1.41 V), due to the higher ORR catalytic kinetics of Mn@HNCNTs-2 (Figure 7a). The polarization curves and power density of the Mn@HNCNTs cell and Pt/C cells are displayed in Figure 7b. As the current density gradually increased from 0 to 200 mA cm⁻², the cell voltage of the Mn@HNCNTs cell is always higher than that of the Pt/C cell. At a current density of 200 mA cm⁻², the Mn@HNCNTs cell delivered a power density of 178 mW cm⁻², also higher than that of the Pt/C cell (142 mW cm⁻²), which further proved that the Mn@HNCNTs cell has an excellent ORR performance in an operational zinc–air cell. The open-circuit voltage and power density of the Mn@HNCNTs cell were also benchmarked against TM/CNT-based air cathodes reported in the literature (Table S3, Supporting Information). It shows that the Mn@HNCNTs cell is one of the best in class. At a current density of 10 mA cm⁻², both the Mn@HNCNTs cell and Pt/C cell could deliver stable cell voltage of 1.30 and 1.15 V, respectively (Figure 7c). The Mn@HNCNTs cell could retain this cell voltage for 20 h, longer than Pt/C, indicating that the Mn@HNCNTs cell has a higher capacity than the Pt/C cell. The voltage responses of both cells at various current densities are shown in Figure 7d. With the increase of the current density, the cell voltages of the Mn@HNCNTs cell were always higher than that of the Pt/C cell. When the current density reverted to 1 mA cm⁻², the cell voltage of the Mn@HNCNTs cell returned to its initial value, demonstrating the robustness and satisfactory rate performance of the Mn@HNCNTs cell as the air cathode in a zinc–air cell.

To further demonstrate the practical application of the assembled Mn@HNCNTs-2 cell, the Mn@HNCNTs-2 cell was used to illuminate the LED light (Figure 7e,f) and recharged by refilling the Zn foil for three times. At a current density of 10 mA cm⁻², the cell voltage of the Mn@HNCNTs-2 cell remained at 1.2 V without any observable drop, indicating good stability. These tests, carried out in zinc–air cells, confirmed that Mn@HNCNTs-2 is an excellent ORR catalyst, which can even deliver a better electrocatalytic performance as the air cathode in the zinc–air cell than the Pt/C.

To better understand why the Mn@HNCNTs-2 has excellent ORR properties, X-ray photoelectron spectroscopy (XPS) analysis for surface properties and chemical states was carried out and displayed in Figure S8 in the Supporting Information. In the XPS survey spectra shown in Figure S8a in the Supporting Information, the signals of C 1s, O 1s, and N 1s were detected in Mn@HNCNTs-2. Since the XPS can only detect elements in the surface depth range of 0.1–10 nm,^[27] no signal of Mn was detected in Mn@HNCNTs-2 (Figure S8b, Supporting Information), this further indicates that the Mn nanoparticles

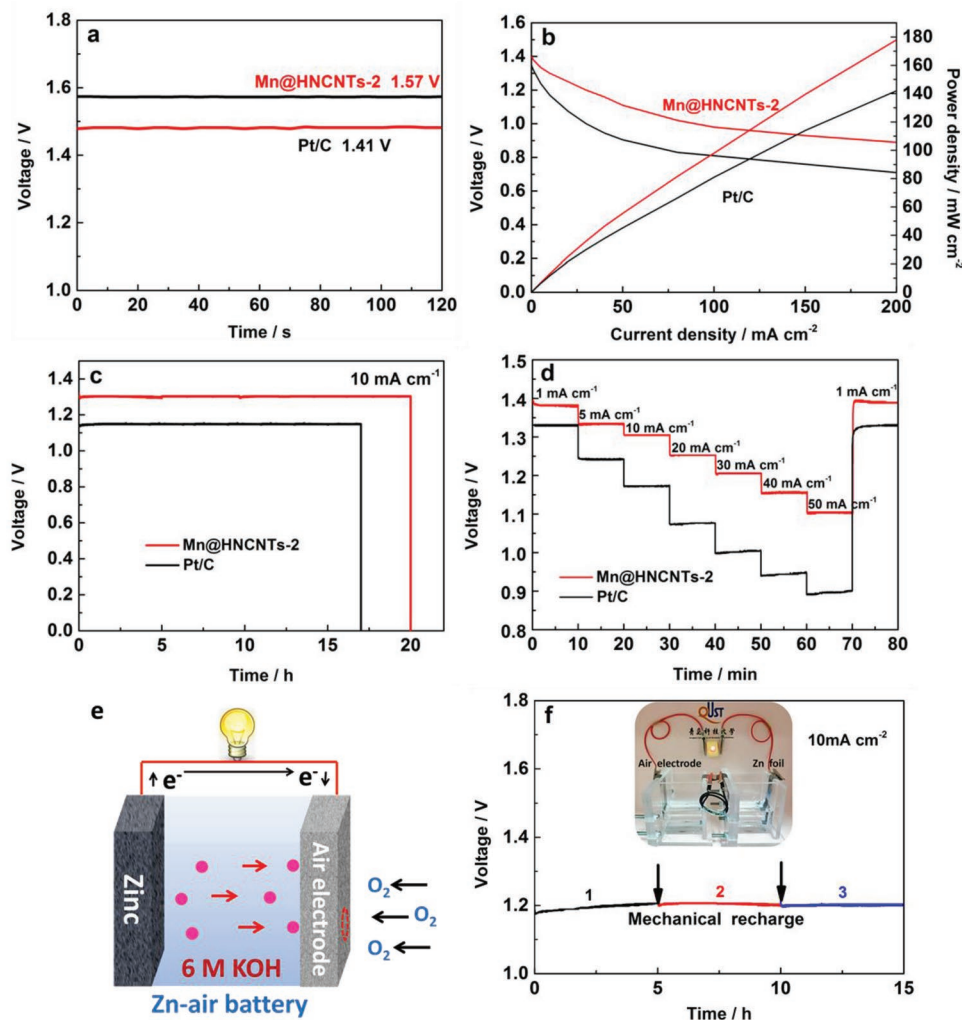


Figure 7. a) Open-circuit voltage of the primary Zn–air cells based on Pt/C and Mn@HNCNTs-2 (electrolyte: 6 M KOH). b) Polarization and power density curves. c) Cell voltage versus time at a current density of 10 mA cm^{-2} . d) Cell voltage versus time at various current densities. e) Schematic diagram of the structure of the assembled zinc–air cell. f) Long-term galvanostatic discharge of an Mn@HNCNTs-2 primary zinc–air cell, which had been recharged by refilling with Zn foil three times.

were completely encapsulated within the carbon matrix. The high-resolution C 1s XPS spectrum of Mn@HNCNTs-2, shown in Figure S8c in the Supporting Information, could be fitted into four peaks at ≈ 284.5 , 285.2 , 286.5 , and 289 eV , which could be ascribed to C=C, C–O/C–N, C=O, and O–C=O, respectively.^[10] The peak at $\approx 285.2 \text{ eV}$ confirmed that nitrogen was doped into the carbon matrix and bonded with carbon. For the nitrogen-doped carbon materials, the nitrogen species available on the surface usually act as the active sites for the electrocatalytic reactions, especially the pyridinic-N and graphitic-N species, which were commonly recognized as the active sites for the N-doped carbon.^[28,29] The pyridinic-N can be found on the edge of a carbon plane. The pyridinic-N is a type of nitrogen that contributes one p-electron to the aromatic p-system and has a lone electron pair in the plane of the carbon matrix, which increase the electron-donating ability of the nitrogen-modified carbon and promotes the process of the ORR.^[30] The graphitic-N is a type of nitrogen that bonds to three carbon atoms in the plane of the carbon matrix. Ikeda et al. found that

the O_2 molecule is preferentially adsorbed at carbon sites on graphene-like zigzag edges if a graphitic-N is located nearby.^[31] The nitrogen-modified carbon-based catalysts developed by Niwa et al.^[32] also shows that the catalysts with a higher content of graphitic-N have higher ORR activity. Based on the above discussion, it could be deduced that the ORR active sites on Mn@HNCNTs-2 derived from the doped nitrogen atoms, namely pyridinic-N and graphitic-N.^[33] The high-resolution N 1s XPS spectrum shown in Figure S8d in the Supporting Information could be deconvoluted into six peaks, namely the peaks at ≈ 398.3 , 399.8 , 401.04 , 402.06 , 404.05 , and 406.02 eV , which correspond to pyridinic-N, pyrrolic-N, graphitic-N, pyridinic N-oxide, $\pi-\pi^*$ satellite and NO_x , respectively.^[10] As shown in the inset of Figure S8d in the Supporting Information, the total amount of pyridinic-N and graphitic-N exposed on the surface of Mn@HNCNTs-2 was more than 30%, which could provide more active sites for the ORR. Based on the above results, it can be deduced that the prevalence of pyridinic-N and graphitic-N on its surface, as well as the high electrochemical surface area, could

provide plenty of active sites to interact with reactants and result in its excellent ORR properties. In addition, to prove the effect of Mn particles on ORR activity of Mn@HNCNTs-2, the catalytic activity of Mn@HNCNTs-2 was compared with that of NCNTs by the LSV in three- and two-electrode systems (Figure S9, Supporting Information). Mn@HNCNTs-2 exhibited better ORR activity than NCNTs (Figure S9c,d, Supporting Information). Mn nanoparticles presented in the carbon material could provide the electron and form more convoluted phase boundaries, which could be another reason the Mn@HNCNTs-2 exhibits good ORR performance in zinc–air cells.

3. Conclusions

In summary, Mn nanoparticles encapsulated within mesoporous helical carbon nanotubes with high surface area can be successfully synthesized in a molten-salt medium of CaCl_2 at 800 °C. The particle size of MnCl_2 catalyst related to ball-milling times played a critical role in forming the helical morphology and porosity. When the ball-milling time was 12 h, the obtained Mn@HNCNTs sample exhibited a high surface area ($424.6 \text{ m}^2 \text{ g}^{-1}$) with plenty of active sites available on its surface. In the real two-electrode primary zinc–air cell, Mn@HNCNTs cell exhibited higher open-circuit voltage of 1.57 V and higher capacity of 178 mW cm^{-2} at 200 mA cm^{-2} than the Pt/C cell (1.41 V , 178 mW cm^{-2}). The Mn@HNCNTs cell also shows a better ORR performance than many reported TM/CNTs in the Zn–air cells. The high ORR activity and low-cost of Mn@HNCNTs-2 make it viable for practical application in the zinc–air battery.

4. Experimental Section

Preparation of Mn@HNCNTs: The synthesis of Mn@HNCNTs was carried out in a molten-salt medium of calcium chloride at high temperature. During the synthesis, melamine was used as the source of both nitrogen and carbon, and manganese chloride tetrahydrate as the precursor of Mn nanoparticles. The detailed synthetic procedure is as follows: 1.562 g of melamine and 0.990 g of manganese chloride tetrahydrate were added into 40 mL of ethanol, and then ultrasonically treated for 30 min. The obtained mixture was heated at 45 °C to evaporate ethanol. The dried powder was mixed with 0.3163 g of calcium chloride. The obtained mixture was transferred into a container with zirconia balls (eight balls with a diameter of 1.0 cm and eight balls with a diameter of 0.5 cm) and ball-milled at the rotating rate of 6000 rpm. The effect of ball-milling time on final morphology and structure was investigated in this study. Samples with ball-milling times of 0, 6, 12, and 18 h were prepared. Subsequently, the ball-milled samples were placed in a ceramic crucible and put in an inert gas furnace. The samples were heat-treated at 800 °C with a heating ramp of $2.5 \text{ }^\circ\text{C min}^{-1}$ and kept at this temperature for 3 h with the protection of a static nitrogen atmosphere. After 3 h, the furnace was cooled to room temperature with a cooling rate of $5 \text{ }^\circ\text{C min}^{-1}$. The obtained samples were then rinsed in 1 M HNO_3 solution for 24 h to remove unstable Mn species. After acid washing, the mixture was washed thoroughly with ultrapure water and dried in a vacuum oven at 60 °C for 12 h. According to the ball-milling times, the final samples were labeled as Mn@HNCNTs-0, Mn@HNCNTs-1, Mn@HNCNTs-2, and Mn@HNCNTs-3, corresponding to the ball-milling times of 0, 6, 12, and 18 h, respectively. Pictures showing what the sample looked like in each step are shown in Figure 2.

Characterization: XRD patterns of the catalysts were recorded on a Shimadzu XD-3A instrument using filtered $\text{Cu-K}\alpha$ radiation ($\lambda = 0.15418 \text{ nm}$), generated at 40 kV and 30 mA. TEM images, high angle annular dark-field scanning transmission electron microscopy (STEM) images, and selected area electron diffraction (SAED) patterns of the catalysts were taken on a JEOL (JEM-2000 FX) microscope operating at 200 kV. X-ray photoelectron spectra (XPS) were acquired with a VG Escalab210 spectrometer fitted with an Mg 300 W X-ray source. Raman spectra were recorded on an RFS 100 FT-Raman spectroscopy (Bruker) with a 532 nm excitation laser beam. BET method was employed to determine specific surface areas for obtained carbon materials, and the pore size distribution was calculated by a density functional theory (DFT) method using a slit pore NLDFT equilibrium model on a Quantachrome Autosorb-iQ volumetric analyzer. The particle size distribution was measured using a nanoparticle analyzer from Malvern, UK, and each sample was tested three times with ten cycles per test. Elemental Analysis was measured by Organic Elemental Analyzer (Thermo Flash2000).

Electrochemical Measurements: ORR electrochemical performance tests were carried out in a conventional three-electrode cell on a CHI760D electrochemical analyzer (CH Instruments). The working electrode was prepared as follows: 5 mg of catalyst was dispersed into 1 mL Nafion/ethanol solution (0.25 wt%) by ultrasonic mixing for 30 min. 8 μL of ink containing 40 mg catalyst were dropped onto the surface of a polished glass-carbon rotating disc electrode (catalyst loading: 0.204 mg cm^{-2}) and air-dried. For performance comparison, commercial Pt/C (20 wt% Johnson Matthey) catalysts were used for the preparation of working electrodes according to the same procedure. Ag/AgCl in saturated KCl was chosen as a reference electrode and Pt wire (ORR) as a counter electrode. 0.1 M KOH purged with N_2 for 30 min was used as the electrolyte for all electrochemical tests in this study. All potential values recorded in the study were converted to potentials versus RHE using the following equation: $E_{\text{RHE}} = E_{\text{working electrode versus Ag/AgCl}} + 0.059 \text{ pH} + E_{\text{Ag/AgCl}}$. *iR* curve compensation was done in the tests and ORR curves were adjusted to take capacitive effects into account. The durability testing of ORR was carried out by continuous cyclic voltammetry in the potential range of 0.036–1.164 V versus RHE at a scan rate of 50 mV s^{-1} in KOH electrolyte for 3000 and 6000 cycles. As-prepared carbon materials were used as cathodes and Zn foil as the anode in a two-electrode cell system. In order to precisely measure specific capacity, the Zn foil electrode was tailored to a width of 1 cm, smoothened, and polished before each test. The air cathode was prepared by dispersing 2 mg of the catalyst, 3 μL of polymer binder (PTFE), 1 mg acetylene black, and 4 mg carbon in 300 μL isopropyl alcohol to form a homogenous slurry. After rolling into a slice and oven drying at 80 °C, the air cathode mixture was pressed onto Ni foam under 20 MPa. For comparison, 2 mg of commercial Pt/C (20 wt% Johnson Matthey) catalysts were prepared as air cathodes.

Supporting Information

Supporting Information is available from the Wiley Online Library or from the author.

Acknowledgements

The authors would like to thank the National Natural Science Foundation of China (21766032 and 51661008) for financially supporting this work.

Conflict of Interest

The authors declare no conflict of interest.

Keywords

helical N-doped carbon nanotube, mesoporous, Mn nanoparticle, oxygen reduction reaction, zinc–air battery

Received: August 10, 2019

Revised: September 14, 2019

Published online: November 7, 2019

-
- [1] X. Zheng, J. Wu, X. Cao, J. Abbott, C. Jin, H. Wang, P. Strasser, R. Yang, X. Chen, G. Wu, *Appl. Catal., B* **2019**, 241, 442.
- [2] C. He, J. Tao, *Adv. Sustainable Syst.* **2018**, 2, 1700136.
- [3] H. Wang, X. Zhang, R. Wang, S. Ji, W. Wang, Q. Wang, Z. Lei, *J. Power Sources* **2011**, 196, 8000.
- [4] J. Ding, S. Ji, H. Wang, D. J. L. Brett, B. G. Pollet, R. Wang, *Chem. - Eur. J.* **2019**, 25, 2868.
- [5] Y. Jiao, Y. Zheng, M. Jaroniec, S. Z. Qiao, *Chem. Soc. Rev.* **2015**, 44, 2060.
- [6] H. Yang, H. Li, H. Wang, S. Ji, J. Key, R. Wang, *J. Electrochem. Soc.* **2014**, 161, F795.
- [7] R. Wang, H. Li, S. Ji, H. Wang, Z. Lei, *Electrochim. Acta* **2010**, 55, 1519.
- [8] Y. Ma, H. Wang, H. Feng, S. Ji, X. Mao, R. Wang, *Electrochim. Acta* **2014**, 142, 317.
- [9] F. Su, Z. Tian, C. K. Poh, Z. Wang, S. H. Lim, Z. Liu, J. Lin, *Chem. Mater.* **2010**, 22, 832.
- [10] J. Ding, S. Ji, H. Wang, H. Gai, F. Liu, B. G. Pollet, R. Wang, *Chem. Commun.* **2019**, 55, 2924.
- [11] Y. Chen, S. Ji, H. Wang, V. Linkov, R. Wang, *Int. J. Hydrogen Energy* **2018**, 43, 5124.
- [12] J. Ding, S. Ji, H. Wang, V. Linkov, H. Gai, F. Liu, Q. Liu, R. Wang, *ACS Sustainable Chem. Eng.* **2019**, 7, 3974.
- [13] H. Wang, T. Maiyalagan, X. Wang, *ACS Catal.* **2012**, 2, 781.
- [14] A. Zhu, L. Qiao, P. Tan, Y. Ma, W. Zeng, R. Dong, C. Ma, J. Pan, *Appl. Catal., B* **2019**, 254, 601.
- [15] Z. Ma, H. Zhang, Z. Yang, G. Ji, B. Yu, X. Liu, Z. Liu, *Green Chem.* **2016**, 18, 1976.
- [16] X. Cui, P. Ren, D. Deng, J. Deng, X. Bao, *Energy Environ. Sci.* **2016**, 9, 123.
- [17] J. Ding, S. Ji, H. Wang, V. Linkov, R. Wang, *J. Power Sources* **2019**, 423, 1.
- [18] J. Ding, P. Wang, S. Ji, H. Wang, V. Linkov, R. Wang, *Electrochim. Acta* **2019**, 296, 653.
- [19] K. Gong, F. Du, Z. Xia, M. Durstock, L. Dai, *Science* **2009**, 323, 760.
- [20] W. J. Lee, U. N. Maiti, J. M. Lee, J. Lim, T. H. Han, S. O. Kim, *Chem. Commun.* **2014**, 50, 6818.
- [21] Z. Ren, P. X. Gao, *Nanoscale* **2014**, 6, 9366.
- [22] S. Amelinckx, X. B. Zhang, D. Bernaerts, X. F. Zhang, V. Ivanov, J. B. Nagy, *Science* **1994**, 265, 635.
- [23] J. Chen, F. Wang, Y. Qian, *Mod. Min.* **2015**, 559, 107.
- [24] T. Zhou, H. Wang, S. Ji, V. Linkov, R. Wang, *J. Power Sources* **2014**, 248, 427.
- [25] J. Ding, S. Ji, H. Wang, H. Gai, F. Liu, V. Linkov, R. Wang, *Int. J. Hydrogen Energy* **2019**, 44, 2832.
- [26] M. Wang, C. Zhang, T. Meng, Z. Pu, H. Jin, D. He, J. Zhang, S. Mu, *J. Power Sources* **2019**, 413, 367.
- [27] H. Niu, Y. Wang, X. Zhang, Z. Meng, Y. Cai, *ACS Appl. Mater. Interfaces* **2012**, 4, 286.
- [28] Y. Qiu, X. Zhang, S. Yang, *Phys. Chem. Chem. Phys.* **2011**, 13, 12554.
- [29] D. Hulicova-Jurcakova, M. Kodama, S. Shiraishi, H. Hatori, Z. H. Zhu, G. Q. Lu, *Adv. Funct. Mater.* **2009**, 19, 1800.
- [30] G. Liu, X. Li, P. Ganesan, B. N. Popov, *Appl. Catal., B* **2009**, 93, 156.
- [31] T. Ikeda, M. Boero, S. F. Huang, K. Terakura, M. Oshima, J. I. Ozaki, *J. Phys. Chem. C* **2008**, 112, 14706.
- [32] H. Niwa, K. Horiba, Y. Harada, M. Oshima, T. Ikeda, K. Terakura, J. Ozaki, S. Miyata, *J. Power Sources* **2009**, 187, 93.
- [33] T. Sharifi, G. Hu, X. Jia, T. Wagberg, *ACS Nano* **2012**, 6, 8904.